

# Axisymmetric MHD simulations of the collapsar model for gamma-ray bursts

Daniel Proga<sup>1</sup>, Andrew I. MacFadyen<sup>2</sup>, Philip J. Armitage<sup>1,3</sup>, and Mitchell C. Begelman<sup>1,3</sup>

<sup>1</sup>JILA, University of Colorado, Boulder, CO 80309-0440, USA

<sup>2</sup>California Institute of Technology, Mail Code 130-33, Pasadena, CA 91125

<sup>3</sup>also Department of Astrophysical and Planetary Sciences, University of Colorado, Boulder

submitted to ApJ Letters on Aug. 28 2003

Received \_\_\_\_\_; accepted \_\_\_\_\_

## ABSTRACT

We present results from axisymmetric, time-dependent magnetohydrodynamic (MHD) simulations of the collapsar model for gamma-ray bursts. We begin the simulations after the  $1.7 M_{\odot}$  iron core of a  $25 M_{\odot}$  presupernova star has collapsed and study the ensuing accretion of the  $7 M_{\odot}$  helium envelope onto the central black hole formed by the collapsed iron core. We consider a spherically symmetric progenitor model, but with spherical symmetry broken by the introduction of a small, latitude-dependent angular momentum and a weak radial magnetic field. Our MHD simulations include a realistic equation of state, neutrino cooling, photodisintegration of helium, and resistive heating. Our main conclusion is that, within the collapsar model, MHD effects alone are able to launch, accelerate and sustain a strong polar outflow. We also find that the outflow is Poynting flux-dominated, and note that this provides favorable initial conditions for the subsequent production of a baryon-poor fireball.

*Subject headings:* accretion, accretion disks – gamma rays: bursts – methods: numerical – MHD – stars: winds, outflows

## 1. Introduction

The collapsar model is one of most promising scenarios to explain the huge release of energy in a matter of seconds, associated with gamma-ray bursts (GRBs; Woosley 1993; Paczyński, 1998; MacFadyen & Woosley 1999, hereafter MW; Popham, Woosley & Fryer 1999; MacFadyen, Woosley & Heger 2001). In this model, the collapsed iron core of a massive star accretes gas at a high rate ( $\sim 1M_{\odot} \text{ s}^{-1}$ ) producing a large neutrino flux, a powerful outflow, and a GRB. Despite many years of intensive theoretical studies of these events, basic properties of the central engine are uncertain. In part, this is because previous numerical studies of the collapsar model did not explicitly include magnetic fields, although they are commonly accepted as a key element of accretion flows and outflows.

In this letter we present a study of the time evolution of magnetohydrodynamic (MHD) flows in the collapsar model. This study is an extension of existing models of MHD accretion flows onto a black hole (BH; Proga & Begelman 2003, PB03 hereafter). In particular, we include a realistic equation of state (EOS), photodisintegration of bound nuclei and cooling due to neutrino emission. Our study is also an extension of MW’s collapsar simulations, as we consider very similar neutrino physics and initial conditions but solve MHD instead of hydrodynamical equations.

## 2. Method

To calculate the structure and evolution of an accreting flow, we solve the equations of MHD:

$$\frac{D\rho}{Dt} + \rho \nabla \cdot \mathbf{v} = 0, \tag{1}$$

$$\rho \frac{D\mathbf{v}}{Dt} = -\nabla P - \rho \nabla \Phi + \frac{1}{4\pi} (\nabla \times \mathbf{B}) \times \mathbf{B}, \tag{2}$$

$$\rho \frac{D}{Dt} \left( \frac{e}{\rho} \right) = -P \nabla \cdot \mathbf{v} + \eta_r \mathbf{J}^2 - \mathcal{L}, \quad (3)$$

$$\frac{\partial \mathbf{B}}{\partial t} = \nabla \times (\mathbf{v} \times \mathbf{B} - \eta_r \mathbf{J}), \quad (4)$$

where  $\rho$  is the mass density,  $P$  is the total gas pressure plus radiation pressure,  $\mathbf{v}$  is the fluid velocity,  $e$  is the internal energy density,  $\Phi$  is the gravitational potential,  $\mathbf{B}$  is the magnetic field vector,  $\mathbf{J}$  is the current density,  $\eta_r$  is an anomalous resistivity, and  $\mathcal{L}$  is the cooling rate due to neutrinos.

To compute resistivity, we follow Stone & Pringle (2001, see their equations 5 and A1). We perform simulations using the pseudo-Newtonian potential of the central mass  $\Phi_{pw} = GM/(r - R_S)$ , where  $R_S = 2GM/c^2$  is the Schwarzschild radius, introduced by Paczyński & Wiita (1980). We increase the mass of the BH during the calculation by the amount of baryonic rest mass accreted through the inner boundary.

Our calculations are performed in spherical polar coordinates  $(r, \theta, \phi)$ . We assume axial symmetry about the rotational axis of the accretion flow ( $\theta = 0^\circ$  and  $180^\circ$ ). The computational domain is defined to occupy the radial range  $r_i = 1.5 R_S \leq r \leq r_o = 1000 R_S$ , and the angular range  $0^\circ \leq \theta \leq 180^\circ$ . The  $r - \theta$  domain is discretized on a non-uniform grid as in PB03, which yields  $\Delta r/r = 0.278$  at the inner edge of the simulations.

We adopt a realistic EOS, which includes contributions from an ideal gas of nuclei, radiation, and electrons and positrons with arbitrary degrees of relativity and degeneracy (Blinnikov, Dunina-Barkovskaya & Nadyozhin 1996). To compute the cooling rate, we follow Itoh et al. (1989, 1990), taking into account thermal neutrino emission processes dominated by pair annihilation, as well as the capture of pairs on free nucleons.

Our calculations use the ZEUS-2D code described by Stone & Norman (1992a,b). We have extended the code to include the realistic EOS, artificial resistivity, photodisintegration

and neutrino cooling. We included the terms due to the resistivity and cooling in an operator split fashion separately from the rest of the dynamical equations. For stability, these terms must be integrated using the time step computed based on the resistive and cooling time scales, respectively. We subcycle whenever either of these two time steps is smaller than the time step used in the MHD equations (see, e.g., Stone, Pringle, and Begelman 1999). Inclusion of a non-adiabatic EOS requires iterating over temperature,  $T$  (see MW for details).

By including the neutrino cooling and realistic EOS, we consider very similar microphysics to that used in MW. Our simulations differ from those in MW in that we use the ZEUS MHD code whereas MW used the PROMETHEUS hydrodynamics code (Fryxell, Müller & Arnett 1989). This means that we can self-consistently calculate turbulent stresses generated by the magnetorotational instability (MRI) and thus include the outward transport of energy and angular momentum (e.g., Balbus & Hawley 1991). MW implemented the effects of viscosity in the disk using an alpha viscosity as prescribed by Shakura & Sunyaev (1973). We do not consider self-gravity and nuclear burning; however, as in MW our simulations track the photodisintegration of helium. Our simulations span the radial direction from 1.5 to 1000  $R_S$  whereas MW’s simulations span from 9.5 to 9500  $R_S$ . Thus we can capture the innermost part of the flow near the BH but follow the evolution out to a smaller radius than MW’s simulations.

We adopt PB03’s boundary conditions and initial conditions for the magnetic field. In particular, the initial magnetic field is purely radial and weak ( $\beta \equiv 8\pi P/B^2 \gg 1$  everywhere). For the initial conditions of the fluid variables, we follow MW and adopt the stellar model for the helium core of a 25  $M_\odot$  presupernova star (model S251S7B@14233 in Woosley & Weaver 1995). The masses of the helium and iron core derived from this star are 7.23 and 1.70  $M_\odot$ , respectively. Similarly to MW’s simulations, our simulations start after

the entire iron core is assumed to have collapsed to form a BH (with  $R_S = 4.957 \times 10^5$  cm), but before the helium envelope has collapsed. The model predicts an inner radius of the helium envelope,  $R_{\text{He}}$ , of  $2.11 \times 10^8$  cm. Outside this radius, we adopt the radial velocity from the stellar model, set  $v_\theta = 0$  and assume a non-zero  $l$ . The angular momentum distribution is chosen such that the ratio between the centrifugal force and the component of gravity perpendicular to the rotational axis is 0.02 at all angles and radii, except where this prescription results in  $l > l_{max} = 10^{17}$  cm<sup>2</sup> s<sup>-1</sup>; then we set  $l = l_{max}$ . Inside  $R_{\text{He}}$ , we set  $v_\theta = v_\phi = 0$  and assume a free-fall radial velocity. We compute the initial density inside the helium envelope using the mass continuity equation and the mass accretion rate from the stellar model at  $R_{\text{He}}$ , where  $\rho = 1.16 \times 10^7$  g cm<sup>-3</sup> and  $v_r = -8.81 \times 10^7$  cm s<sup>-1</sup>.

### 3. Results

With these assumptions, there is only one free parameter which defines the strength of the initial magnetic field. In this letter, we present results from a single model for which  $\beta = 10^6$  at the outer boundary.

We find that after a transient episode of infall, lasting 0.13 s, the gas with  $l \gtrsim 2R_S c$  piles up outside the black hole and forms a thick torus bounded by a centrifugal barrier near the rotation axis. Soon after the torus forms (i.e., a couple of orbits at  $r = r_i$ ), the magnetic field is amplified by both MRI and shear. We have verified that most of the inner torus is unstable to MRI, and that our simulations have enough resolution to resolve, albeit marginally, the fastest growing MRI mode. The torus starts evolving rapidly and accretes onto the black hole. Another important effect of magnetic fields is that the torus produces a magnetized corona and an outflow. The presence of the corona and outflow is essential to the evolution of the inner flow at all times and the entire flow close to the rotational axis during the latter phase of the evolution. We find that the outflow very quickly becomes

sufficiently strong to overcome supersonically infalling gas (the radial Mach number in the polar funnel near the inner radius is  $\sim 5$ ) and makes its way outward, reaching the outer boundary at  $t = 0.25$  s. Due to limited computing time, our simulations were stopped at  $t = 0.28215$  s, which corresponds to 6705 orbits of the flow near the inner boundary. We expect the accretion to continue much longer, roughly the collapse timescale of the Helium core ( $\sim 10$  s), as in MW.

Figure 1 shows the time evolution of the mass accretion rate through the inner boundary (left panel), total magnetic energy (second left panel), neutrino luminosity (third left panel) and radial Poynting and kinetic flux along the polar axis at  $r = 190 R_S$  (right panel). Unless otherwise stated, all quantities in this paper are in cgs units. Initially, during a precollapse phase,  $\dot{M}_a$  stays nearly constant at the level of  $\sim 5 \times 10^{32}$  g s $^{-1}$ . During this phase the zero- $l$  gas inside the initial helium envelope is accreted. Around  $t = 0.13$  s,  $\dot{M}_a$  rises sharply as the gas from the initial helium envelope reaches the inner boundary. However, this gas has non-zero  $l$  and a rotational supported torus and its corona and outflow form, causing a drop in  $\dot{M}_a$  after it reaches a maximum of  $2 \times 10^{33}$  g s $^{-1}$  at  $t = 0.145$  s. The accretion rate reaches a minimum of  $6 \times 10^{31}$  g s $^{-1}$  at  $t \approx 0.182$  s and then fluctuates with a clear long-term increase. This increase is caused by the contribution from gas with  $l < 2R_S c$ , which is directly accreted (without need to transport  $l$ ) from outside the main body of the torus. The total mass and angular momentum accreted onto the BH during our simulation (0.3 s) are  $0.1 M_\odot$  and  $3 \times 10^{39}$  g cm $^2$  s $^{-1}$ , respectively.

The time evolution of the total magnetic energy (integrated over the entire computational domain) is characteristic of weakly magnetized rotating accretion flows. Most of the magnetic energy is due to the toroidal component of the magnetic field. We note a huge increase of the toroidal magnetic field coinciding with the formation and development of the torus. Both  $B_\phi$  and  $B_\theta$  are practically zero during the precollapse

phase of the evolution. But at  $t = 0.14$  s the total energy in  $B_\phi$  equals that in  $B_r$  and just 0.025 s later the  $B_\phi$  energy is higher than the  $B_r$  energy by a factor of 50. At the end of simulations the total kinetic energy from the radial, latitudinal and rotational motion are  $4 \times 10^{50}$ ,  $6.5 \times 10^{49}$ , and  $2.3 \times 10^{51}$  erg, respectively. These gross properties indicate that the magnetic energy is large enough to play an important role in the flow dynamics.

The time evolution of the neutrino luminosity,  $L_\nu$ , shows that the neutrino emission stays at a relatively constant level of  $3 \times 10^{52}$  erg s $^{-1}$  after the torus forms. We compute  $L_\nu$  under the assumption that all the gas in the model is optically thin to neutrinos, so that  $L_\nu$  is volume integrated  $\mathcal{L}$  over the entire computational domain. We note that  $L_\nu$  is dominated by the neutrino emission due to pair capture on free nucleons (the so-called URCA cooling).

The last panel in Fig. 1 shows the area-integrated radial fluxes of magnetic and kinetic energy at  $r = 190 R_S$  inside the polar outflow. The outflow is Poynting flux-dominated, with the Poynting flux exceeding the kinetic energy flux by up to an order of magnitude.

Our analysis of the inner flow shows that the outflow is magnetically driven from the torus. Soon after the torus forms, the magnetic field very quickly deviates from its initial radial configuration due to MRI and shear. This leads to fast growth of the toroidal magnetic field as field lines wind up due to the differential rotation. As a result the toroidal field dominates over the poloidal field and the gradient of the former drives an outflow. Figure 2 shows the flow pattern of the inner part of the flow at  $t = 0.2735$  s. The left and right panel show density and  $|B_\phi|$  maps, respectively. The maps are overlaid by the direction of the poloidal velocity. The polar regions of low density and high  $B_\phi$  coincide with the region of an outflow. We note also that during the latter phase of the evolution not all of the material in the outflow originated in the innermost part of the torus – a significant part of the outflow is “peeled off” the infalling gas at large radii by the magnetic



pressure. Figure 2 illustrates that the inner torus and its corona and outflow cannot always prevent the low- $l$  gas from reaching the BH. Even the magnetic field cannot do it if the density of the incoming gas is too high. Therefore, we find that the outflow of the magnetic energy (mostly toroidal) from the innermost part of the flow does not always correspond to an outflow of gas (in other words, the Poynting flux and kinetic energy flux can be in opposite directions).

Figure 3 shows the radial profiles of several quantities in our run, angle-averaged over a small wedge near the equator (between  $\theta = 86^\circ$  and  $94^\circ$ ), and time-averaged over 50 data files covering a period at the end of the simulations (from 0.2629 s through 0.2818 s). We indicate the location of the last stable circular orbit by the vertical dotted line in each panel.

The profiles of each variable are not simple power-laws but are rather complex. In particular, the density has a prominent maximum of  $4 \times 10^{11} \text{ g cm}^{-3}$  at  $r = 5R_S$ . The gas plus radiation pressure is higher than the magnetic pressure. The rotational velocity is nearly Keplerian inside  $r = 6R_S$  and sub-Keplerian outside this radius.

We measure the Reynolds stress,  $\alpha_{gas} \equiv \langle \rho v_r \delta v_\phi \rangle / P$ , and the Maxwell stress normalized to the magnetic pressure,  $\alpha_{mag} \equiv \langle 2B_r B_\phi / B^2 \rangle$ . Note that Figure 3 shows only the magnitude, not the sign, of the normalized stresses. We find that except for  $r \lesssim 2.5R_S$  and  $10R_S \lesssim r \lesssim 12R_S$ , the Maxwell stress dominates over the Reynolds stress in the inner flow. The last panel in Figure 3 shows that the toroidal component of the magnetic field is dominant for  $r < 50 R_S$ .

We have compared the cooling time scale and the advection time scale in the flow and found that overall the flow is advection-dominated except for a small region inside the torus where the density reaches its maximum.

#### 4. Discussion and Conclusions

We have performed time-dependent two-dimensional MHD simulations of the collapsar model. Our simulations show that: 1) soon after the rotationally supported torus forms, the magnetic field very quickly starts deviating from purely radial due to MRI and shear. This leads to fast growth of the toroidal magnetic field as field lines wind up due to the torus rotation; 2) The toroidal field dominates over the poloidal field and the gradient of the former drives a polar outflow against supersonically accreting gas through the polar funnel; 3) The polar outflow is Poynting flux-dominated; 4) The polar outflow reaches the outer boundary of the computational domain ( $5 \times 10^8$  cm) with an expansion velocity of  $0.2c$ ; 6) The polar outflow is in a form of a relatively narrow jet (when the jet breaks through the outer boundary its half opening angle is  $5^\circ$ ); 7) Most of the energy released during the accretion is in neutrinos,  $L_\nu = 2 \times 10^{52}$  erg  $s^{-1}$ . Therefore it is likely that neutrino driving can increase the outflow energy (e.g., Fryer & Mészáros 2003 and references therein).

Our simulations explore a relatively conservative case where we allow for neutrino emission but do not allow for the emitted neutrinos to interact with the gas or annihilate. The only sources of nonadiabatic heating in our simulations are the artificial viscosity and resistivity.

Our main conclusion is that, within the collapsar model, MHD effects are able to launch, accelerate and sustain a strong polar outflow. We believe that this conclusion will turn out to be largely independent of the initial magnetic field strength in the stellar core, because MRI can rapidly amplify weak fields until they are strong enough to drive a powerful outflow. Since our simulations are non-relativistic, and cover only the innermost region of the collapsing star, we cannot determine whether our outflows are sufficient to yield a GRB. Additional driving could also be necessary. We also find that the outflow is Poynting flux-dominated, and note that this provides favorable initial conditions for

the subsequent production of a baryon-poor fireball [e.g., Fuller, Pruet & Abazajian (2000); Beloborodov (2003); Vlahakis & Königl (2003); Mészáros (2002)], or a magnetically dominated “cold fireball” [Lyutikov & Blandford (2002)].

ACKNOWLEDGMENTS: DP acknowledges support from NASA under LTSA grants NAG5-11736 and NAG5-12867. MCB acknowledges support from NSF grants AST-9876887 and AST-0307502.

## REFERENCES

- Balbus, S. A., & Hawley, J. F. 1991, *ApJ*, 376, 214
- Beloborodov, A.M. 2003, *ApJ*, 588, 931
- Blinnikov, S.I., Dunina-Barkovskaya, N.V., & Nadyozhin, D. K. 1996, *ApJS*, 106, 171
- Fuller, G. M., Pruet, J., & Abazajian, K. 2000, *Phys. Rev. Lett.*, 85, 2673
- Fryxell, B. A., Müller, E., & Arnett, W. D. 1989, MPA Rep. 449 (Garching: MPA)
- Fryer, C. L., & Mészáros, P. 2003, *ApJ*, 588, L25
- Itoh, N., Adachi, T., Nakagawa, M., Kohyama, Y., & Munakata, H. 1989, *ApJ*, 339, 354
- Itoh, N., Adachi, T., Nakagawa, M., Kohyama, Y., & Munakata, H. 1990, *ApJ*, 360, 741
- Lyutikov, M. & Blandford, R. 2002, *APS, APR*, 6008
- MacFadyen, A., & Woosley, S.E. 1999, *ApJ*, 524, 262 (MW)
- MacFadyen, A., Woosley, S.E., & Heger A. 2001, *ApJ*, 550, 410
- Mészáros, P. 2002, *ARA&A*, 40, 137
- Paczynski, B. 1998, *ApJ*, 494, L45
- Paczynski, B., & Wiita, P. J. 1980, *A&A*, 88, 23 (PW)
- Popham, R., Woosley, S.E., & Fryer, C. 1999, *ApJ*, 518, 356
- Proga, D., & Begelman, M.C. 2003 *ApJ*, 592, 767 (PB03)
- Shakura, N.I., & Sunyaev, R.A. 1973 *A&A*, 24, 337

Stone, J.M., & Norman, M.L. 1992a, ApJS, 80, 753

Stone, J.M., & Norman, M.L. 1992b, ApJS, 80, 791

Stone, J. M., & Pringle, J. E. 2001, MNRAS, 322, 461

Stone, J.M., Pringle, J.E., & Begelman, M.C. 1999, MNRAS, 310, 1002

Vlahakis, N., & Königl, A. 2003, ApJ, submitted

Woosley, S.E. 1993, ApJ, 405, 273

Woosley, S. E., & Weaver, T. A. 1995, ApJS, 101, 181

### Figure Captions

Figure 1 – The time evolution of the mass accretion rate (left panel), total magnetic energy due to each of the three field components (second left panel), neutrino luminosity (third left panel) and area-integrated radial Poynting and kinetic flux in the polar outflow at  $r = 190 R_S$  (right panel). Formally, we define the polar outflow as the region where  $v_r > 0$  and  $\beta < 1$ . Note the difference in the time range in the panel with the radial fluxes.

The last panel in Fig. 1 shows the area-integrated radial fluxes of magnetic and kinetic energy at  $r = 190 R_S$  inside the polar outflow. Formally, we define the polar outflow as the region where  $v_r > 0$  and  $\beta < 1$ . The outflow is Poynting flux-dominated, with the Poynting flux exceeding the kinetic energy flux by up to an order of magnitude.

Figure 2 – Color maps of logarithmic density and toroidal magnetic field overplotted with the direction of the poloidal velocity at  $t = 0.2735$  s. The length scale is in units of the BH radius (i.e.,  $r' = r/R_S$  and  $z' = z/R_S$ ).

Figure 3 – Radial profiles of various quantities from our run, time-averaged from 0.2629 through 0.2818 s. To construct each plot, we averaged the profiles over angle between  $\theta = 86^\circ$  and  $94^\circ$ . The top left panel plots the density (solid line) and temperature (dashed line). The top middle panel plots the gas pressure (solid line) and magnetic pressure. The top right panel plots the rotational, radial, Keplerian, and Alfvén velocities (solid, dashed, dot-dashed, and dotted line, respectively), as well as the sound speed (triple-dot dashed line). The bottom left panel plots the angular velocity in units of  $2c/R_s$ . The bottom middle panel plots the Maxwell stress,  $\alpha_{mag}$ , and the Reynolds stress,  $\alpha_{gas}$  (solid and dashed line, respectively). We calculate the Reynolds stress using eq. (15) in PB03 and show only

its amplitude. The bottom right panel plots the radial, latitudinal and toroidal components of the magnetic field (dot-dashed, dashed, and solid line, respectively). The length scale is in units of the BH radius (i.e.,  $r' = r/R_S$ ).

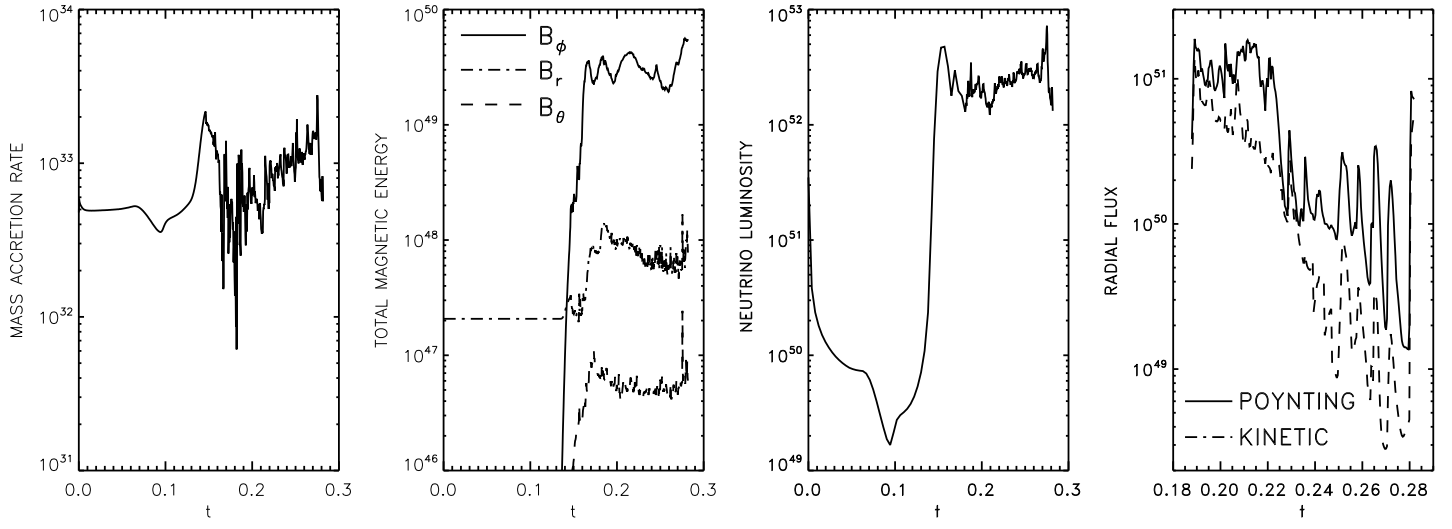


Fig. 1.—



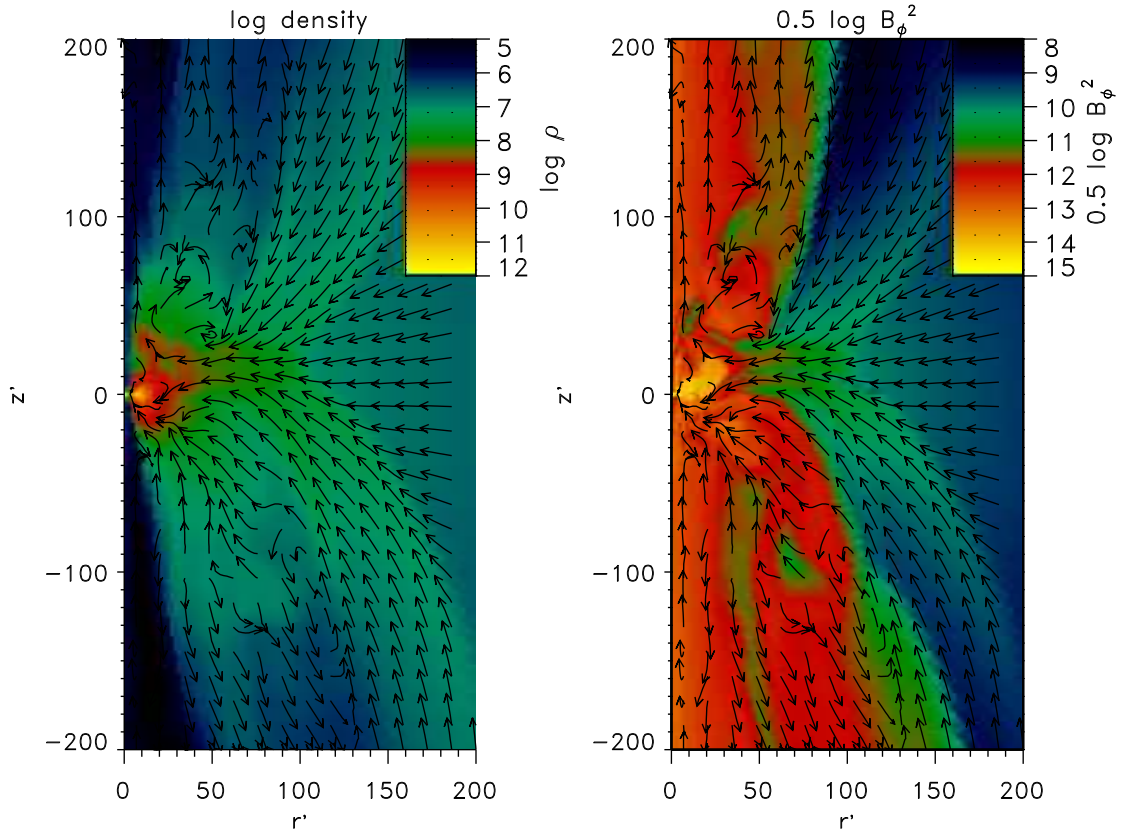


Fig. 2.—

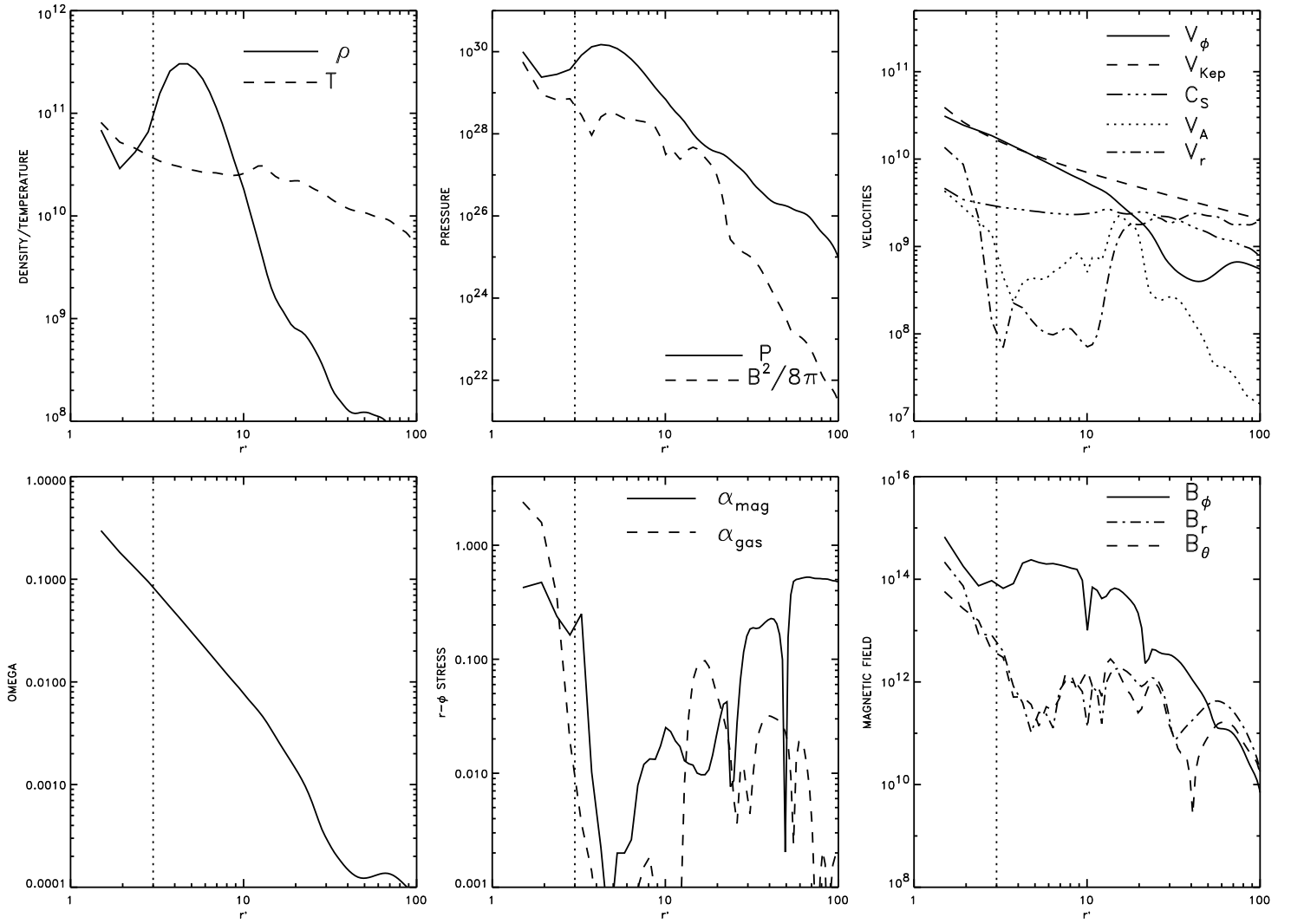


Fig. 3.—